Oceanic Impetus for Convective Onset of the Madden–Julian Oscillation in the Western Indian Ocean

ADAM V. RYDBECK

American Society for Engineering Education, Washington, D.C.

TOMMY G. JENSEN

Oceanography Division, Naval Research Laboratory, Stennis Space Center, Stennis Space Center, Mississippi

(Manuscript received 15 August 2016, in final form 13 February 2017)

ABSTRACT

A theory for intraseasonal atmosphere–ocean–atmosphere feedback is supported whereby oceanic equatorial Rossby waves are partly forced in the eastern Indian Ocean by the Madden–Julian oscillation (MJO), reemerge in the western Indian Ocean ~70 days later, and force large-scale convergence in the atmospheric boundary layer that precedes MJO deep convection. Downwelling equatorial Rossby waves permit high sea surface temperature (SST) and enhance meridional and zonal SST gradients that generate convergent circulations in the atmospheric boundary layer. The magnitude of the SST and SST gradient increases are 0.25°C and 1.5°C Mm^{-1} (1 megameter is equal to 1000 km), respectively. The atmospheric circulations driven by the SST gradient are estimated to be responsible for up to 45% of the intraseasonal boundary layer convergence observed in the western Indian Ocean. The SST-induced boundary layer convergence maximizes 3–4 days prior to the convective maximum and is hypothesized to serve as a trigger for MJO deep convection. Boundary layer convergence is shown to further augment deep convection by locally increasing boundary layer moisture. Warm SST anomalies facilitated by downwelling equatorial Rossby waves are also associated with increased surface latent heat fluxes that occur after MJO convective onset. Finally, generation of the most robust downwelling equatorial Rossby waves in the western Indian Ocean is shown to have a distinct seasonal distribution.

1. Introduction

The Madden–Julian oscillation (MJO) is a coupled phenomenon wherein momentum, heat, and moisture are continually exchanged between the atmosphere and ocean. The MJO propagates eastward at approximately 5 m s^{-1} in the Indian Ocean and is defined by large-scale regions of enhanced and suppressed convection (Madden and Julian 1972). Low-level convergence occurs immediately to the east of deep convection and low-level divergence occurs to the west (Hendon and Salby 1994; Maloney and Hartmann 1998; Kiladis et al. 2005; Benedict and Randall 2007). Recent studies have hypothesized that oceanic equatorial waves are responsible for the initiation of select MJO events by locally increasing surface latent and sensible heat fluxes that destabilize the atmosphere for deep convection (Webber et al. 2010, 2012a,b). In addition to confirming the importance of warm SSTs and increased surface latent heat fluxes for MJO convection, we show that oceanic equatorial waves strengthen SST gradients that drive low-level convergence that may act as a trigger for MJO convection in the western Indian Ocean.

Two oceanic equatorial wave types are associated with forcing from, as well as forcing of, the MJO: the Kelvin and the equatorial Rossby (ER) wave (Enfield 1987; Hendon et al. 1998; Kessler and Kleeman 2000; Han et al. 2001; Shinoda and Hendon 2002; Roundy and Kiladis 2006; Webber et al. 2010; Oliver and Thompson 2010; Gribble-Verhagen and Roundy 2010; Iskandar and McPhaden 2011; Webber et al. 2012a,b; Shinoda et al. 2013; Gottschalck et al. 2013; Seiki et al. 2013; Webber et al. 2014; Jensen et al. 2015). Forcing from the MJO occurs when westerly wind stress on the equator forces mass convergence, positive sea surface height (SSH) anomalies, downwelling that corresponds to a depressed thermocline, and increased ocean heat

Corresponding author e-mail: Adam V. Rydbeck, adam.rydbeck.ctr@nrlssc.navy.mil

DOI: 10.1175/JCLI-D-16-0595.1

TABLE 1. The data sources, grid spacing, and temporal coverage are shown for the data used in the composite analyses.

Variable	Grid spacing and time period
AVISO SSH	0.25 × 0.25; 1993–2014
Version-7 TRMM Multisatellite Precipitation Analysis	0.25 × 0.25; 1993–2013
NOAA OLR	2.5 × 2.5; 1993–2013
ERAI winds and specific humidity	0.75 × 0.75; 1993–2013
TropFlux surface fluxes	0.75 × 0.75; 1993–2013
NOAA daily optimum interpolation SST V2 from the Advanced Very High Resolution Radiometer (AVHRR) and Advanced Microwave Scanning Radiometer for Earth Observing System (AMSR-E)	0.25 × 0.25; June 2002–October 2011 using AVHRR and AMSR-E data; remainder of 1993–2013 using AVHRR data only

content (OHC; Webber et al. 2010, 2012a; Shinoda et al. 2013; Jensen et al. 2015). These anomalies propagate eastward as a downwelling Kelvin wave. First-baroclinic-mode Kelvin wave phase speeds are 2.8–3.2 m s^{-1} in the Indian Ocean (e.g., Gent et al. 1983; Jensen 1993; Shinoda et al. 2009). ER waves can also be directly forced by equatorial wind stress (Schott and Quadfasel 1983; Battisti 1988; Delcroix et al. 1991). ER waves straddle the equator and modulate mass divergence, SSH, SST, currents, thermocline depth, and OHC. In addition to MJO wind stress, Kelvin and ER waves are forced by semiannual westerly wind stress that develops in the equatorial Indian Ocean during the intermonsoon months of April–May and October–November (Wyrtki 1973; O'Brien and Hurlburt 1974; Jensen 1993; Han et al. 1999).

Westward-propagating downwelling ER waves have been observed to coincide with the initiation of primary MJO events in the western Indian Ocean (Webber et al. 2010, 2012a,b). In this context, primary MJO events are those that do not have antecedent convective signals to the west. The following series of events describes the atmosphere–ocean–atmosphere feedback for MJO convective onset theorized by Webber et al. (2010). Downwelling Kelvin waves forced by MJO wind stress propagate eastward in the Indian Ocean. These waves reflect off the coast of Sumatra as coastal Kelvin and ER waves. The ER waves propagate westward and, upon arrival in the western Indian Ocean ~90 days later, deepen the thermocline. The deeper thermocline prevents mixing of colder water from beneath the mixed layer. SST and surface heat fluxes increase, and the atmosphere destabilizes leading to MJO convective onset. The SST warming of +0.3°C associated with downwelling ER waves is comparable to the magnitude of SST warming that precedes MJO convection in the Indian Ocean and west Pacific (Shinoda et al. 1998; Woolnough et al. 2000; de Szoeke et al. 2015; DeMott et al. 2016). While warm SST anomalies that lead MJO convection are largely regulated by net surface heat fluxes, warm SST anomalies associated with downwelling ER waves and MJO initiation are hypothesized to be strongly regulated by additional processes that are local to the western Indian Ocean.

Certain climatological features of the western Indian Ocean make it particularly sensitive to oceanic variations capable of initiating intraseasonal convection. In addition to a climatologically warm sea surface, a zonal region of Ekman divergence and upwelling in the tropical southwest Indian Ocean forces a collocated region of shallow thermocline depths known as the Seychelles–Chagos thermocline ridge (SCTR; Hermes and Reason 2008 and references therein). Xie et al. (2002) noted a high correlation between thermocline depth and SST in the SCTR indicating the importance of subsurface ocean dynamics to SST in the region. For example, downwelling ER waves deepen the thermocline and assist the local warming of SST (Webber et al. 2010, 2012a).

This study expands on previous work detailing mechanisms by which MJO convection may be initiated by oceanic ER waves in the western Indian Ocean. While previous studies have utilized an MJO index to examine oceanic ER waves, the present study utilizes an oceanic ER wave index to examine the MJO. A description of the oceanic wave index and the data used are presented in section 2. Section 3 examines the relationship of ER waves to the MJO and hypothesizes a mechanism for MJO initiation by examining composites of atmospheric and oceanic variables. Section 4 examines the evolution of the vertically integrated moisture budget of the atmospheric boundary layer in the western Indian Ocean as a function of the ER wave life cycle. In section 5, the results are summarized, and conclusions are presented.

2. Data and compositing methods

Data used in this study, including the grid spacing and time intervals, are shown in Table 1. Merged sea surface height (SSH) anomalies using multiple satellite-borne altimeters available from the Archiving, Validation, and

Interpretation of Satellite Oceanographic Data (AVISO; Pascual et al. 2006) are used to calculate the ER wave index. The ER wave index is described in the next paragraph and is used for compositing oceanic and atmospheric variables. The version-7 Tropical Rainfall Measuring Mission (TRMM) Multisatellite Precipitation Analysis 3B42 precipitation product (Huffman et al. 2007) and the National Oceanic and Atmospheric Administration (NOAA) outgoing longwave radiation (OLR) data (Liebmann and Smith 1996) are used to analyze rainfall and convective patterns associated with ER waves in the Indian Ocean. The latter is used as a proxy for convection owing to its extended temporal coverage. Atmospheric variables from the European Centre for Medium-Range Weather Forecasts interim reanalysis (ERA-Interim, hereafter ERAI; Dee et al. 2011) are used to calculate the moisture budget and analyze low-level wind patterns. TropFlux surface flux estimates (Kumar et al. 2012) are also used to analyze intraseasonal surface fluxes. TropFlux uses bias-corrected ERAI data as input to calculate fluxes from the Coupled Ocean–Atmosphere Response Experiment (COARE), version 3.0, algorithm. Finally, NOAA daily Optimum Interpolation SST, version 2, data (Reynolds et al. 2007) are used to document the emergence of warm SST anomalies and enhanced SST gradients associated with downwelling ER waves in the western Indian Ocean. All data are daily. To assist the identification of MJO events, the real-time multivariate MJO index (RMM) of Wheeler and Hendon (2004) is utilized (http://www.bom.gov.au/climate/mjo/graphics/rmmm.74toRealtime.txt). The RMM is based on the leading pair of empirical orthogonal functions for the combined fields of 850-hPa zonal wind, 200-hPa zonal wind, and OLR.

Composite fields are based on an ER wave index that isolates SSH anomalies associated with westward-propagating oceanic ER waves in the Indian Ocean. The ER wave index is calculated from SSH. First, SSH is filtered in wavenumber–frequency space to remove variability outside of 50–500-day periods and wavenumbers −1 to −30. The filtering bounds capture westward-propagating variability, including annual and semiannual ER waves known to occur in the Indian Ocean (e.g., Han et al. 1999). The 50-day cutoff is selected to suppress variability associated with tropical instability waves. In Fig. 1, filtered SSH anomalies averaged from 6°S to 6°N are shown for years 2004–08. Westward-propagating waves dominated by a semiannual periodicity are observed. The waves generally originate in the eastern Indian Ocean, consistent with ER waves that are initiated by reflected Kelvin waves.

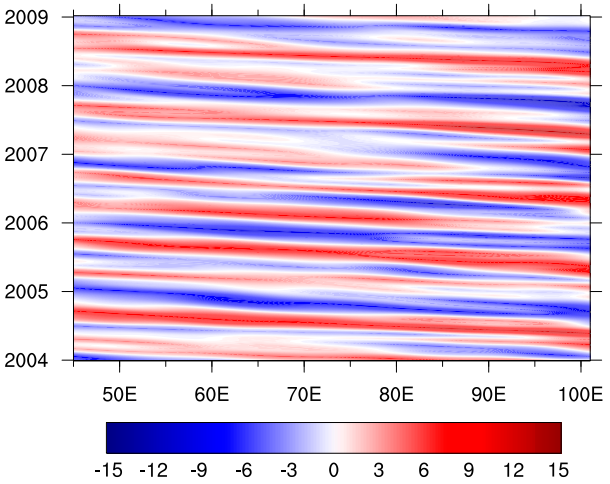

FIG. 1. SSH anomalies (cm) filtered in wavenumber–frequency space. The SSH anomalies are filtered to isolate ER waves that reside between wavenumbers −1 and −30 and periods of 50–500 days. SSH anomalies are then averaged from 6°S to 6°N and shown for the years 2004–08.

This is also supported in section 3 (shown in Fig. 4 below). After confirming the efficacy of the wavenumber–frequency filtering, SSH anomalies are then averaged over the latitude–longitude box of 6°S–6°N, 59°–69°E and are normalized by the standard deviation. Symmetric latitude bands from 10°N to 10°S were tested in half-degree increments to find those most appropriate for capturing ER wave propagation along the equator. The index is sensitive to whether the averaging box captures the meridional extent of ER waves and their region of reemergence in the western Indian Ocean. A time series of the ER wave index is shown in Fig. 2. Filtered data near the ends of the time series (within 500 days) are ignored in the index and not shown in Fig. 2. Maxima of the ER wave index greater than 1.5 standard deviations are considered strong downwelling ER wave events and used throughout the study for compositing. The use of 1.5 standard deviations as the cutoff results in a reasonable sample size of the strongest ER waves in the western Indian Ocean (16 ER wave events). Lowering the threshold to include more events does not detract from the major conclusions of the investigation but generally weakens the composite variable amplitudes.

The dates for the 16 ER wave events are shown in Table 2. The dates are clustered about a few months during boreal summer and winter. In boreal summer, events predominantly occur from July through mid-August with an additional event in June. In boreal winter, ER wave events occur from mid-January through February. These dates occur 2–3 months after the intermonsoon

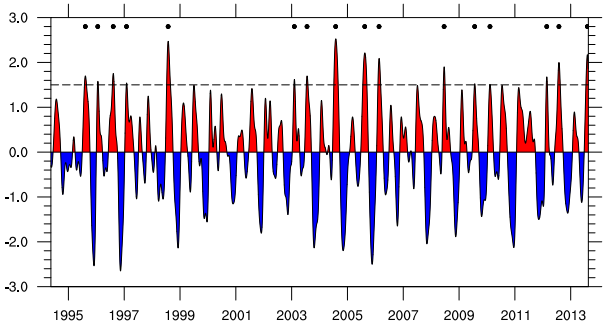

FIG. 2. The ER wave index for the western Indian Ocean. The index is computed by filtering SSH anomalies to isolate equatorial Rossby wave signals that reside between wavenumbers −1 and −30 and periods of 50–500 days. SSH anomalies are then averaged over 6°S–6°N, 59°–69°E and normalized. Maxima of the index that exceed 1.5 standard deviations are considered robust downwelling ER waves and are used for compositing. These events are indicated by black dots.

TABLE 2. The dates are local maxima in the ER wave index that exceed 1.5 standard deviations. The SSH anomalies used to create the ER wave index are averaged within 6°S–6°N, 59°–69°E and normalized. The index is based on SSH anomalies filtered to retain variability in 50–500-day periods and westward-propagating wavenumbers 1–30. These dates are used for compositing and correspond to lag 0.

Equatorial Rossby wave events	
Boreal summer	Boreal winter
7 Aug 1995	17 Jan 1996
7 Aug 1996	25 Jan 1997
26 Jul 1998	2 Feb 2003
18 Jul 2003	15 Feb 2006
28 Jul 2004	6 Feb 2010
12 Aug 2005	19 Feb 2012
16 Jun 2008	
21 Jul 2009	
28 Jul 2012	
4 Aug 2013	

periods in the Indian Ocean (April–May and October–November) during which westerly surface wind stress forces downwelling Kelvin waves. These results suggest that semiannual Kelvin waves are at least partly responsible for producing ER waves that coherently propagate into the western Indian Ocean several months later (see Figs. 1, 3 and 4). Lag composites, used throughout the study, are generated relative to the dates shown in Table 2, defined as lag 0 day. The next section provides support that the semiannual forcing of ER waves is reinforced by the MJO in the central and eastern Indian Ocean.

3. Remote forcing by oceanic equatorial Rossby waves

In this section, composites of atmospheric and oceanic variables based on the ER wave index are examined. The evolution of downwelling ER waves, relationship

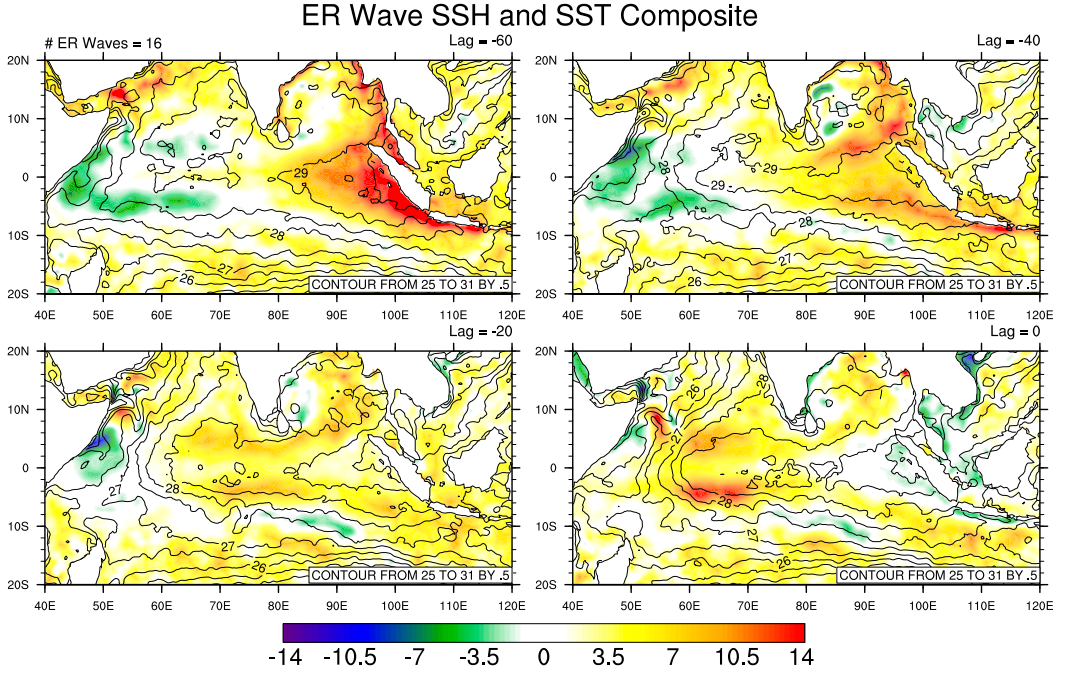

FIG. 3. Composites of SSH anomalies (color; cm) and SST (contours; °C) for lags −60, −40, −20, and 0 days. SST contours range from 26° to 31°C with a 0.5°C contour interval.

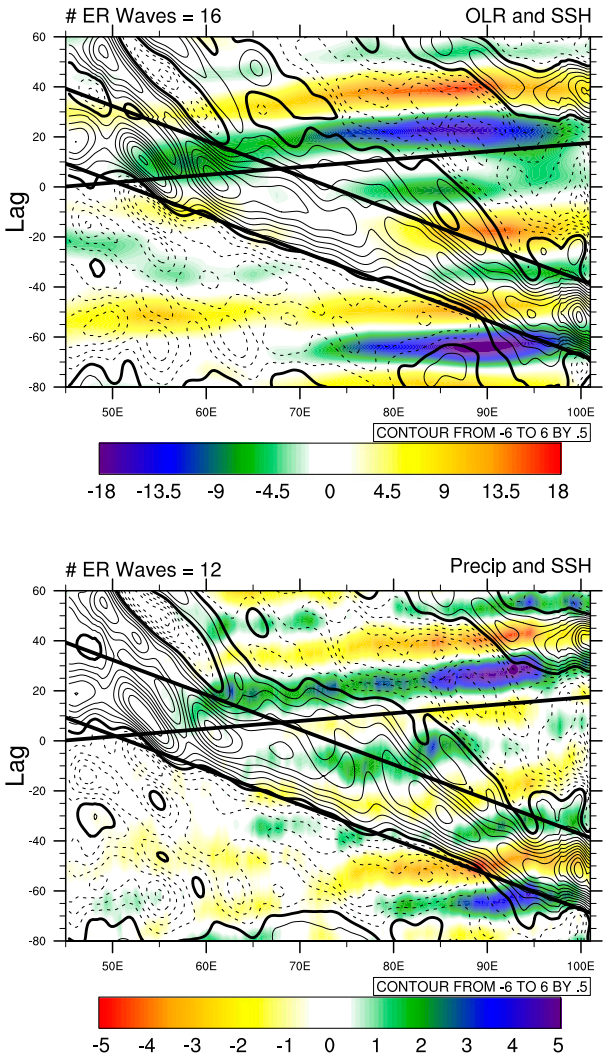

FIG. 4. (top) The 20–200-day bandpass-filtered OLR (color; $W m^{-2}$) and SSH (contours; cm) anomaly composites. (bottom) Precipitation (color; $mm day^{-1}$) and bandpass-filtered SSH (contours; cm) anomalies. Anomalies are averaged between 2° and 6°S and between 2° and 6°N. SSH contours range from −6 to +6 cm with a 0.5-cm contour interval. The abscissa is longitude (°) and the ordinate is lag (days) relative to the ER wave index. The number of ER wave events used in the composite is shown in the upper left of each panel. The eastward phase line is $4.0 m s^{-1}$, and the westward phase lines are $0.9 m s^{-1}$.

of ER waves to the MJO, and role of ER waves in driving boundary layer convergence are described in this section. Many features of ER waves and the MJO have previously been described (Webber et al. 2010, 2012a,b). The present study deviates from prior studies in several important aspects: the method of identifying the relationship between ER waves and the MJO is new, observations of the predecessor MJO event that leads to the development of ER waves are presented, the phase speed of ER waves crossing the Indian Ocean agrees with theory, and the mechanism of MJO convective onset forced by ER waves in the western Indian Ocean is novel. For these reasons, the details of downwelling ER waves in the Indian Ocean are reexamined.

a. ER wave life cycle

Lag composites of SSH and SST over the ER wave life cycle are shown in Fig. 3. At lag −60 days, increased SSH in the eastern Indian Ocean associated with the downwelling portion of an equatorial Kelvin wave is impinging on the coast of Sumatra. At this time, downwelling coastal Kelvin waves are observed propagating northward along the Bay of Bengal and southward along the coasts of Sumatra and Java. Southward-propagating coastal Kelvin waves have been suggested as being important to modulating the Indonesian Throughflow (Shinoda et al. 2016). In the western Indian Ocean, negative SSHs associated with upwelling ER waves are observed straddling the equator between the 2° and 6° latitude bands immediately west of 70°E.

In the eastern Indian Ocean at lag −40 days, positive SSHs are associated with downwelling ER waves that straddle the equator near 90°E and poleward-propagating coastal Kelvin waves. A tongue of warm SST (>29°C) is present across much of the equatorial Indian Ocean. By lag −20 days, the downwelling ER waves have propagated westward and are roughly centered near 75°E. These waves are not as readily identifiable in SSH in the central Indian Ocean. However, positive SSH anomalies of just a few centimeters are associated with increased thermocline depths of tens of meters (e.g., Kessler et al. 1995; McPhaden 1999). Zonal SST gradients develop in the western Indian Ocean indicated by the "tightening" of sea surface isotherms. By lag 0 days, SSH maxima associated with downwelling ER waves are observable in the western Indian Ocean. Along the equator in the western Indian Ocean, going from west to east, the SST dramatically increases from 26° to 28.5°C in ~10° longitude. A tight packing of isotherms is also present on the poleward edges of the downwelling ER waves. Compared to lag −60 days, the isotherms in the western Indian Ocean have been pulled equatorward in both the Northern and Southern Hemispheres. Although not readily apparent from Fig. 3, SST has also warmed along the 2°–6° latitudes in the western Indian Ocean (see Figs. 7 and 8 below).

b. Relationship of the ER wave to the MJO

Signals of westward-propagating ER waves are more easily identified when data are filtered. In processing the data, the annual cycle has been removed and a 20–200-day Lanczos filter with 241 symmetric weights has been applied, similar to the methods of capturing ER wave

variability utilized by Webber et al. (2010, 2012a) and MJO variability by Matthews (2008). Figure 4 shows a lag–longitude composite of 20–200-day bandpass-filtered SSH anomalies overlaid on OLR and precipitation anomalies, respectively, averaged over the 2°–6° latitude bands in the Northern and Southern Hemispheres. The method of averaging hemispheric latitude bands (Wheeler and Kiladis 1999) was also used by Webber et al. (2010) to analyze the signals of ER waves. Similar patterns emerge if anomalies are averaged from 6°S to 6°N. However, signals become weaker and less coherent because the composites include strong signals along the equator associated with oceanic Kelvin waves. Figure 4 (top) shows OLR and SSH anomalies composited for the 16 downwelling ER wave events listed in Table 1. SSH anomalies are indicated by the line contours and clearly show a westward-propagating signal that begins in the eastern Indian Ocean near 105°E at lag −55 days. These anomalies propagate westward at 0.9 m s^{-1} indicated by the two phase lines, consistent with the phase speed of the first meridional first baroclinic mode ER wave (Chelton et al. 1998). The ER wave phase speed agrees with the Rossby wave dispersion relation, which prescribes that long Rossby waves propagate at approximately ⅓ the phase speed of Kelvin waves (Matsuno 1966; Webber et al. 2010). The ER wave arrives in the far-western Indian Ocean 75 days later at lag +20 days.

Shortly before ER wave generation in the eastern Indian Ocean, an eastward-propagating OLR minimum is observed (Fig. 4, top). The ~5 m s^{-1} phase speed of the OLR minimum is consistent with MJO phase speeds. The timing of ER wave generation suggests that westerly wind stress associated with the MJO reinforces semiannual westerlies in the Indian Ocean (shown below in Fig. 10), leading to a robust Kelvin wave response. The Kelvin wave signal is confirmed by analysis of equatorial SSH anomalies not included in the latitudinal averaging bands of Fig. 4 (not shown). The westward-propagating positive SSH anomalies associated with the ER wave weaken in the central Indian Ocean, similar to the pattern observed in Fig. 3. As the downwelling ER wave reaches the western Indian Ocean, SSH anomalies generally increase between 50° and 65°E and are associated with ER wave reemergence there. Concurrent with the arrival of ER waves in the western Indian Ocean, an OLR minimum develops. The OLR minimum then propagates eastward at ~4.0 m s^{-1} in the western Indian Ocean as indicated by the phase line in Fig. 4. The OLR minimum appears to accelerate in the central and eastern Indian Ocean, while precipitation anomalies (Fig. 4, bottom) propagate at approximately 4 m s^{-1} across the entire Indian Ocean.

These results are confirmed using TRMM precipitation anomalies (Fig. 4, bottom). Only overlapping years of TRMM and AVISO data (1998–2013) are used in this composite. Although 25% fewer events are included, the TRMM composites largely agree with the composites of OLR. Specifically, TRMM composites show the downwelling SSH anomalies associated with ER waves beginning in the eastern Indian Ocean. Prior to ER wave development, positive intraseasonal precipitation anomalies of 3–4 mm day^{-1} are observed to propagate eastward near lags −70 to −65 days. The downwelling ER wave then reemerges in the western Indian Ocean 70 days later, and eastward-propagating precipitation anomalies of 1–3 mm day^{-1} commence. In both composites, relatively weak composite intraseasonal convective variability is present at lag 0 to −10 days and 75°E, as the ER waves transit the Indian Ocean. Weak intraseasonal convective anomalies in the central Indian Ocean may be related to the development of a small number of MJO events associated with ER waves transiting the central Indian Ocean, as suggested by Shinoda et al. (2013).

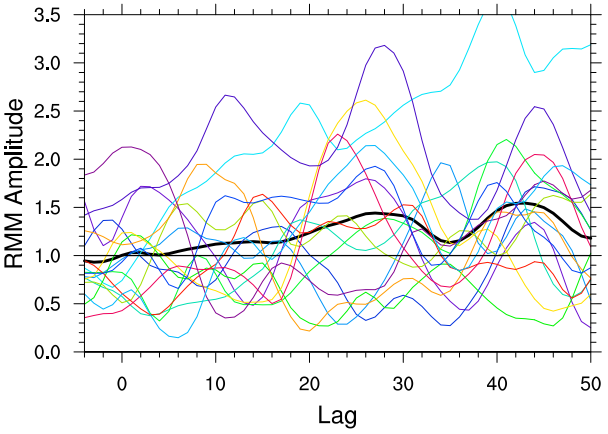

FIG. 5. RMM amplitude for the composite (black) and the 16 events (color) that formulate the composite is shown as a function of lag days.

To confirm that the OLR anomalies in the western Indian Ocean, which develop upon the arrival of downwelling ER waves, are, in fact, associated with the MJO, the RMM index amplitude is composited using the ER wave index and shown in Fig. 5. The composite RMM (bold black line) gradually increases from below 1.00 at lag 0 days to 1.46 at lag +32 days. For the RMM, a threshold of 1.00 is typically used to identify robust MJO events. The composite RMM exceeds 1.00 at lag +5 days and remains above this threshold through lag +50 days. In addition to the MJO events that commence upon the arrival of downwelling ER waves in the western Indian Ocean, the RMM suggests that moderate-amplitude MJO events assist the generation of downwelling ER waves. At lag −60 days when negative OLR anomalies are present in the eastern Indian Ocean (see Fig. 4), the

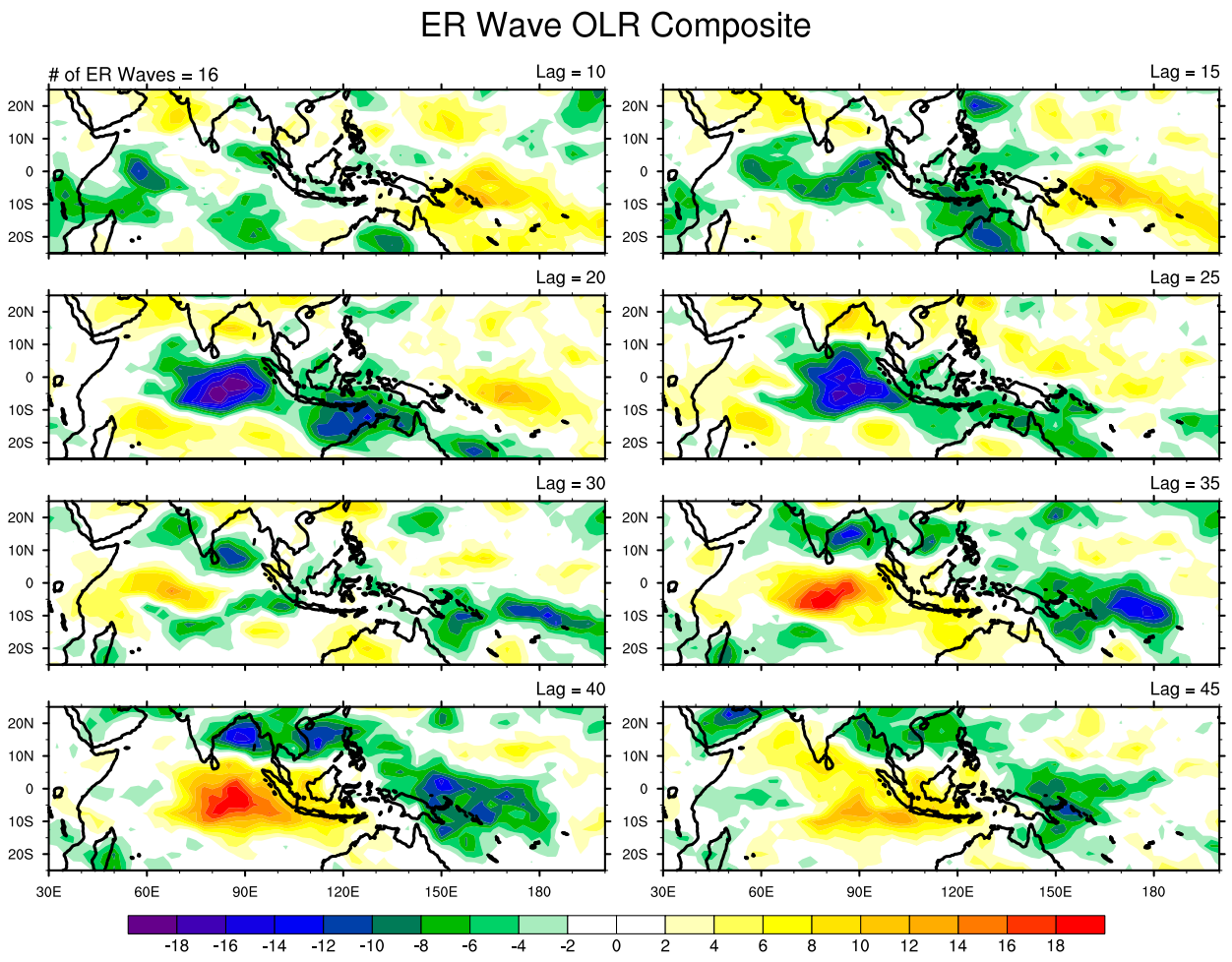

FIG. 6. Composite maps of 20–200-day bandpass-filtered OLR anomalies (W m^{-2}) are shown for lags +10, +15, +20, +25, +30, +35, +40, and +45 days. Composites are based on 16 ER wave events and the lags are shown in the upper right of each panel.

RMM has a value of 1.11 (not shown). From these results, ER waves appear to be forced by the combined westerly wind stress associated with the intermonsoon period and the active phase of the MJO. Approximately 70 days later, MJO initiation is synchronous with the arrival of oceanic ER waves in the western Indian Ocean. Future modeling work is required to determine the relative importance of MJO and intermonsoon wind stress in forcing oceanic equatorial wave responses.

The RMM amplitude for each ER wave event is also shown in Fig. 5. Prior to lag 0 days, the RMM magnitude of 11 events is below 1.00. At lag +25 days, the RMM magnitude of 11 events is above 1.00. The average period that a particular event's RMM amplitude stays above 1.00 is 31 days. The composite RMM is slightly decreased when the strongest event, occurring on 25 January 1997 (light blue line), is removed. With the strongest event removed, the composite RMM magnitude exceeds 1.00 at lag +7 days and remains above the threshold through lag +50 days (figure not shown). While there is considerable spread in the individual RMM magnitudes, the composite RMM appears to be representative of the members and not an artifact of a single outlier.

The evolution of intraseasonal convection associated with downwelling ER waves is further analyzed using lag composite maps of intraseasonal OLR anomalies (Fig. 6). Negative OLR anomalies begin in the equatorial western Indian Ocean at lag +10 days and propagate eastward, growing and intensifying in the central and eastern Indian Ocean at lags +20 and +25 days. At lags +30 and +35 days, negative OLR anomalies in the Indian Ocean weaken and propagate northward into the Bay of Bengal as positive OLR anomalies build along the equator. At lag +40 days, northward-propagating negative OLR anomalies intensify and display a southeast-to-northwest tilt, consistent with patterns of the intraseasonal oscillation during boreal summer (e.g., Wang et al. 2006), eventually weakening at lag +45 days. When

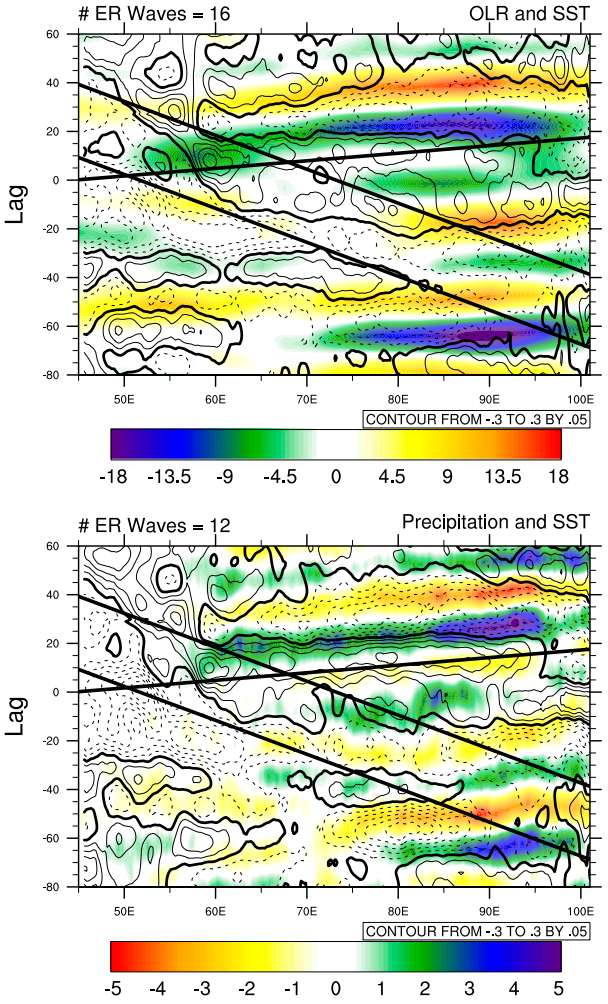

FIG. 7. As in Fig. 4, but for (top) OLR (color; W m^{-2}) and SST (contours; °C) anomalies and (bottom) precipitation (color; mm day^{-1}) and SST (contours; °C) anomalies. The SST contours range from −0.3° to +0.3°C with a 0.05°C contour interval.

ER events are partitioned by season and composited, intraseasonal OLR magnitudes are increased and propagation patterns are more coherent for the respective seasons (not shown), indicating that the patterns of Fig. 6 are a consequence of compositing distinct propagation patterns for varying seasons. In composites of the respective seasons, northeastward propagation in the Indian Ocean and South China Sea is more prominent during boreal summer. During boreal winter, OLR anomalies are predominantly located in the Southern Hemisphere and coherently propagate across the Maritime Continent. Future work is directed at analyzing the seasonal relationship of the ER wave and MJO in the western Indian Ocean.

ER waves in the western Indian Ocean contribute to local SST warming. Figure 7 (top) shows the lag composite of OLR and SST anomalies. SST anomalies do not coherently propagate along the path of ER waves in the Indian Ocean. However, warm SST anomalies emerge in the western Indian Ocean, near 60°E, upon the arrival of ER waves. As mentioned in the introduction, this is possibly due to the regional sensitivity of the climatologically shallow thermocline in the western Indian Ocean. The warm SST anomalies maximize at lag +7 days with values at and above +0.2°C. These SST anomalies are comparable to flux-induced SST anomalies observed in the MJO (Shinoda et al. 1998; de Szoeke et al. 2015) and SST anomalies observed for ER waves using an alternative compositing method (Webber et al. 2010). Broad warming is observed during lags 0–15 days and longitudes 57°–65°E. This warming extends to the east at later lags. The SST maximum at 60°E and lag +7 days is predominantly in phase with the OLR minimum, while warm SST anomalies lead the OLR minimum to the east. (Interestingly, negative OLR anomalies are present near 55°E where a weak negative SST anomaly is present. The relationship between SST gradients and boundary layer convergence discussed below resolves these distinctions.) The phase differences between SST and convective anomalies during MJO onset and propagation in the Indian Ocean are consistent with previous observational studies (Gutzler et al. 1994; Sperber et al. 1997) and suggest that different processes are at play for the initiating and propagating regimes of the MJO.

For the propagating regime of the MJO, warm SST anomalies occur 10–15 days in advance of enhanced convection as a result of increased solar radiation and reduced surface wind speeds (e.g., Flatau et al. 1997; Shinoda et al. 1998; DeMott et al. 2015). In Fig. 7, east of 70°E, the phase relationship of SST and deep convection is typical of the propagating regime. In the MJO initiation region near 60°E and where SST anomalies are warm, incoming solar radiation is reduced and latent heat fluxes are slightly increased (see Fig. 9). Similar phase relationships are observed when examining TRMM precipitation and SST anomalies, though the SST warming is generally greater between lags 0 to +20 days (Fig. 7, bottom). With this in mind, the SST anomalies in the MJO initiation region are, perhaps, more strongly regulated by the thermocline depth in the presence of downwelling ER waves than the surface fluxes. The various roles of the modified SST field in the western Indian Ocean are explored later.

A composite map of 20–200-day bandpass-filtered SST anomalies is shown in Fig. 8 for lags 0, +5, +10, and +15 days. Warm SST anomalies of 0.2°C appear first in the Southern Hemisphere at lag 0 days and 62°E. By lag +5 days, warm anomalies of 0.2°C are present in the Northern Hemisphere and anomalies in the Southern Hemisphere have warmed to 0.3°C. The warm

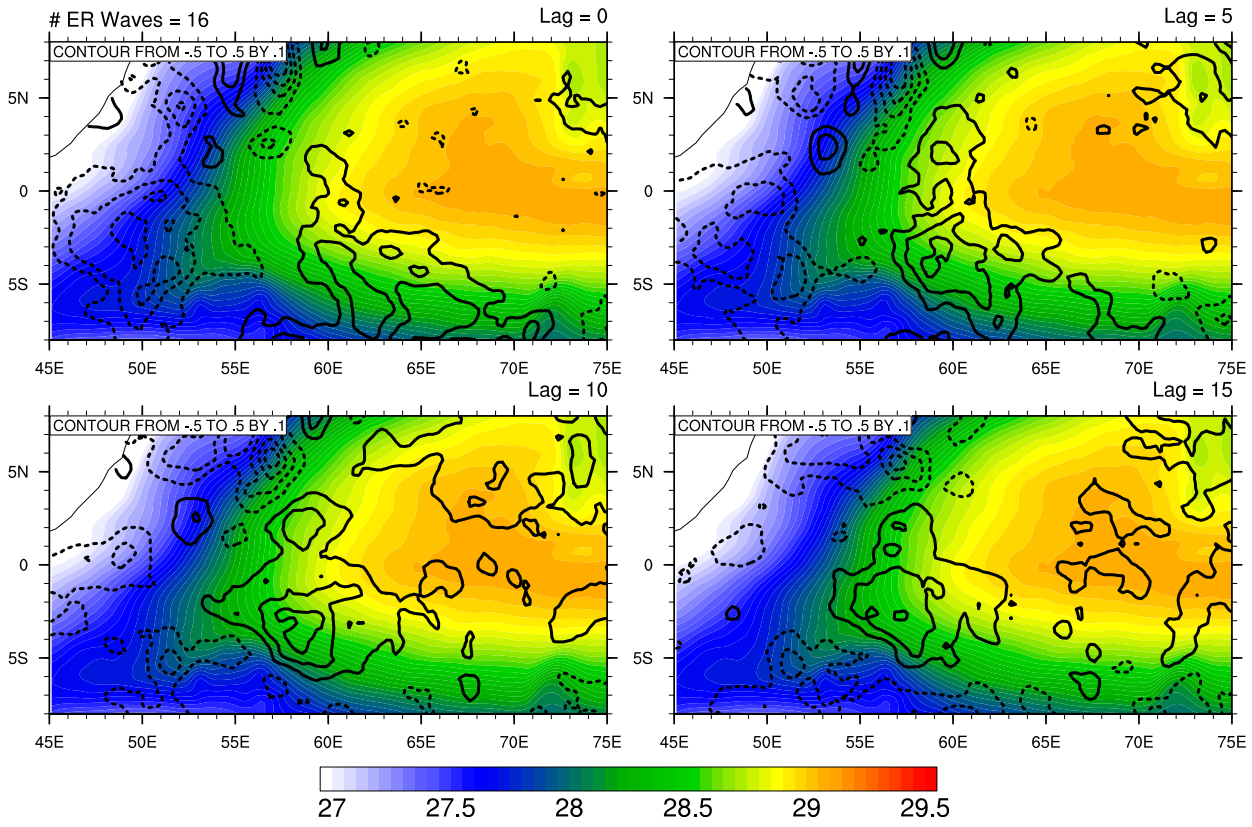

FIG. 8. The composite map of 20–200-day bandpass-filtered SST anomalies (contours; °C) and mean SST (color; °C) are shown for lag 0, +5, +10, and +15 days. The anomalous SST contours range from −0.5° to +0.5°C with a 0.1°C contour interval. Positive contours are solid and negative contours are dashed. The zero contour line is omitted.

anomalies continue to expand over the next 5 days and are located in a transition region between climatologically cool SST to the west and climatologically warm SST to the east. The effect of warm SST anomalies on the total SST is a westward expansion of the Indian Ocean warm pool, also observed in the unfiltered SST of Fig. 3. As will be shown later in Fig. 11, this pattern results in locally increased SST gradients. At lag +15 days, the SST maxima have weakened by ~0.1°C.

Figure 9 shows the relationship of surface latent heat flux and convection anomalies. In the OLR composite (Fig. 9, top) near lag +12 days and 60°E, latent heat fluxes maximize with values of 6 W m^{-2}. The latent heat fluxes maximize a few days after SST at the same longitude. Unlike the warm SST anomalies, positive latent heat flux anomalies of 4–6 W m^{-2} are present immediately to the west of convection and appear to be a response to MJO convective heating that forces surface westerlies to the west of convection. The latent heat flux maximum located at lag +12 days and 60°E slightly lags the OLR minimum. Between 60° and 70°E and from lags +10 to +20 days, latent heat fluxes anomalies are largely in phase with OLR, though the precise phase relationship in this region is difficult to interpret as the OLR minimum is weak. As the MJO propagates farther eastward, latent heat flux anomalies lag MJO convection by ~5 days, as observed near 85°E and lag +28 days, consistent with previous observations of MJO propagation in the Indian Ocean (e.g., Benedict and Randall 2007; DeMott et al. 2015).

Similar phase relationships between latent heat flux and convection anomalies are observed for TRMM (Fig. 9, bottom). Latent heat flux anomalies of +7.5 W m^{-2} near 60°E and lag +13 days are equivalent to moisture anomalies of 0.26 mm day^{-1}. Considering precipitation anomalies around the same time and location are 1.25–2.0 mm day^{-1}, latent heat flux anomalies are ~13%–20% of the magnitude of anomalous precipitation. Regarding MJO theories that fit within the weak temperature gradient approximation in which the MJO is primarily destabilized by moisture, latent heat flux anomalies of this magnitude are hypothesized to be large enough to destabilize the atmospheric column for deep convection (e.g., Araligidad and Maloney 2008; Riley Dellaripa and Maloney 2015). Surface latent heat flux anomalies associated with ER

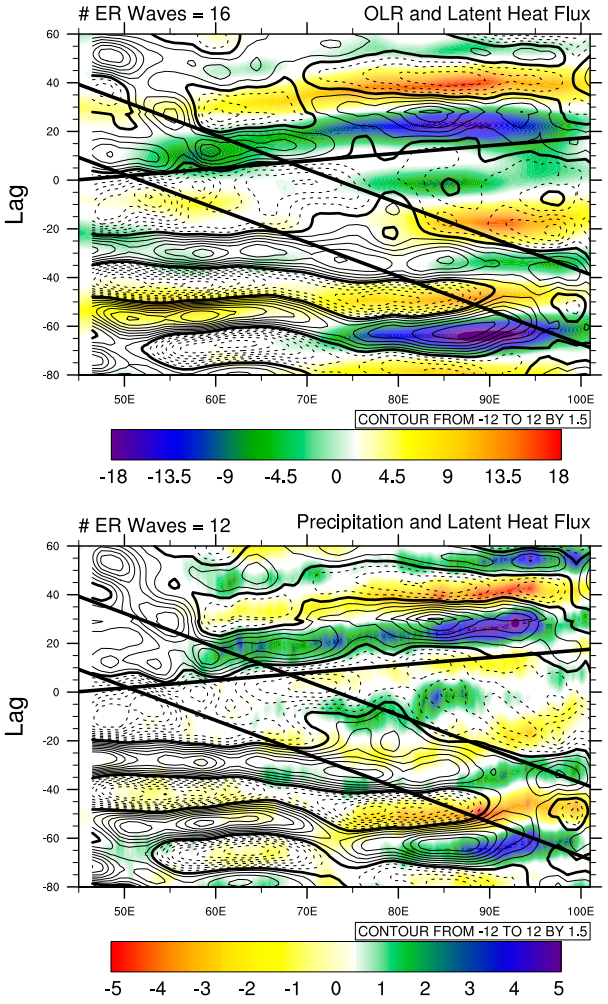

FIG. 9. As in Fig. 7, but for (top) OLR (color; W m^{-2}) and latent heat flux (contours; W m^{-2}) anomalies and (bottom) precipitation (color; mm day^{-1}) and latent heat flux (contours; W m^{-2}) anomalies. The latent heat flux contours range from −12 to +12 W m^{-2} with a 1.5 W m^{-2} contour interval.

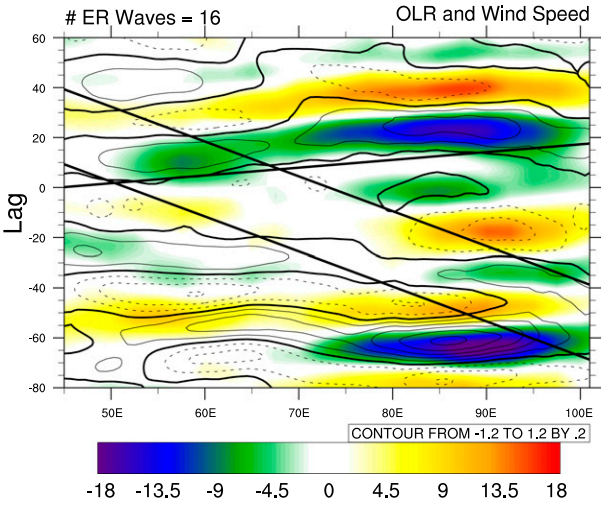

FIG. 10. As in Fig. 9 (top), but for OLR (color; W m^{-2}) and 10-m total wind speed (contours; m s^{-1}) anomaly composites. Wind speed contours range from −1.2 to +1.2 m s^{-1} with a 0.2 m s^{-1} contour interval.

waves are supportive of MJO convection after convective onset but do not appear to be responsible for MJO initiation as suggested by Webber et al. (2010). Consistent with many previous studies (e.g., DeMott et al. 2016), the phasing of latent heat flux anomalies and total wind speed anomalies (Fig. 10) suggests that enhanced latent heat flux anomalies largely result from increased total wind speeds. The contribution from SST variations is secondary. An alternative mechanism for MJO convective initialization resulting from ER waves is hypothesized below.

c. SST-induced boundary layer convergence

ER waves that modulate the SST of the western Indian Ocean are responsible for locally enhancing SST gradients. Many simple models have simulated the process by which SST gradients imprint hydrostatic pressure gradients on the atmospheric boundary layer and drive boundary layer convergence (e.g., Lindzen and Nigam 1987; Back and Bretherton 2009). As is shown below, SST driven boundary layer convergence leads MJO deep convection and is hypothesized to function as a large-scale convective trigger. When calculating the derived boundary layer divergence from the SST field, the divergence is shown to be proportional to the Laplacian of the SST (LSST; or the divergence of the SST gradient vectors). Li and Carbone (2012) showed that ~75% of mesoscale convective rainfall onsets in the tropical west Pacific Ocean occurred in the presence of mesoscale SST gradients. In investigating the roles of boundary layer convergence in the eastward propagation of the MJO, Hsu and Li (2012) estimated that 10%–25% of the boundary layer convergence to the east of MJO convection results from forcing by the SST arrangement. Carbone and Li (2015) observed that the negative LSST was strongly related to the onset of convection in the MJO. They showed that the negative LSST is associated with convective organization on the order of 1000–2000 km (9°–18° longitude). In their findings, negative LSST leads MJO precipitation in the Indian Ocean by 10 to 15 days.

Figure 11 shows ER composites of OLR and SST gradient magnitude |∇SST| anomalies. The maximum of |∇SST| anomalies is located between 55°–60°E at lags −5 to +20 days. The anomalous |∇SST| maximum exceeds 1.5°C Mm^{-1} (1 megameter is equal to 1000 km). A secondary maximum of 0.75°C Mm^{-1} is present to the

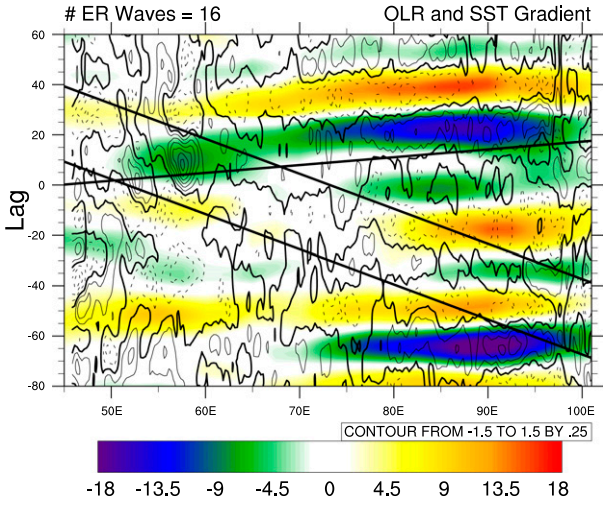

FIG. 11. As in Fig. 10, but for OLR (color; $\mathrm{W\,m^{-2}}$) anomalies and $|\nabla\mathrm{SST}|$ (contours; $^\circ\mathrm{C\,Mm^{-1}}$). The $|\nabla\mathrm{SST}|$ contours range from -1.5° to $+1.5^\circ\mathrm{C\,Mm^{-1}}$ with a $0.25^\circ\mathrm{C\,Mm^{-1}}$ contour interval.

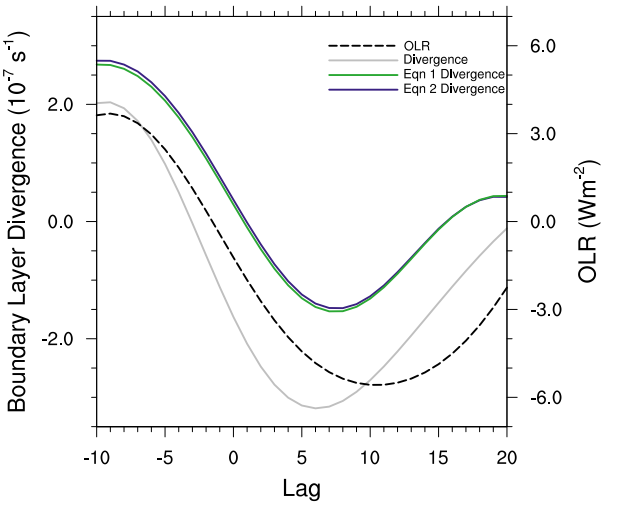

FIG. 12. Composites of 20–200-day bandpass-filtered anomalies of boundary layer divergence (gray; $1\times10^{-7}\,\mathrm{s^{-1}}$), OLR (dashed black; $\mathrm{W\,m^{-2}}$), diagnosed divergence using Eq. (1) (green; $1\times10^{-7}\,\mathrm{s^{-1}}$), and diagnosed divergence using Eq. (2) (blue; $1\times10^{-7}\,\mathrm{s^{-1}}$) averaged over the latitude bands 2°–6°S and 2°–6°N and longitudes 50°–65°E. Composites are based on 16 ER wave events and shown for lags from −10 to +20 days.

west and occurs at slightly earlier lags. The maximum of $|\nabla\mathrm{SST}|$ anomalies coincides with the longitudes of the local minimum of OLR. The $|\nabla\mathrm{SST}|$ maximum is largely a result of the zonal SST gradient that peaks in the same longitude band at lag +5 days with values of $1.25^\circ\mathrm{C\,Mm^{-1}}$ (not shown). The meridional $|\nabla\mathrm{SST}|$ anomalies peak at $0.75^\circ\mathrm{C\,Mm^{-1}}$ near lag +10 days (not shown). Thus the zonal component of the $|\nabla\mathrm{SST}|$ anomaly is first present in the western Indian Ocean and is the strongest. This is somewhat evident in the sea surface isotherm composites of Fig. 3.

To understand the effect of the LSST in forcing boundary layer convergence, two equations are used to diagnose the divergent wind response of the boundary layer to the configuration of SST. The boundary layer divergence is first diagnosed using the boundary layer wind equation of Wang and Li (1993). The investigation of MJO boundary layer convergence by Hsu and Li (2012) also utilized this equation. Since we are primarily interested in the boundary layer divergence that results from the SST field, the free-tropospheric wave effect of the original equation is neglected. With this in mind, the boundary layer divergence may be written as follows:

$$\nabla\cdot\mathbf{U}' = \left[\frac{R}{2}\frac{(p_s-p_e)}{p_e}\Big/\left(\frac{E}{f}+\frac{f}{E}\right)\right]\left[\frac{\partial}{\partial x}\left(\frac{1}{f}\frac{\partial \mathrm{SST}}{\partial x}+\frac{1}{E}\frac{\partial \mathrm{SST}}{\partial y}\right)+\frac{\partial}{\partial y}\left(\frac{1}{f}\frac{\partial \mathrm{SST}}{\partial y}-\frac{1}{E}\frac{\partial \mathrm{SST}}{\partial x}\right)\right]' \quad (1)$$

where $\mathbf{U}$ is the boundary layer horizontal wind, R is the gas constant for dry air, p_e is the pressure at the top of the boundary layer (850 hPa), p_s is the pressure at the bottom of the boundary layer (1000 hPa), f is the Coriolis parameter, and E is the frictional coefficient ($1\times10^{-4}\,\mathrm{s^{-1}}$). Primes indicate bandpass-filtered terms. Neglecting the Coriolis force when deriving Eq. (1) does not significantly alter the solution shown in Fig. 12.

The boundary layer divergence is also diagnosed using the equation from Li and Carbone (2012):

$$\nabla\cdot\mathbf{U}' = \left(\frac{gH_e\Delta t}{T_b}\nabla^2\mathrm{SST}\right)', \quad (2)$$

where g is the acceleration due to gravity, H_e is the effective boundary layer depth, Δt is the characteristic transport time, and T_b is the mean boundary layer temperature. In the calculation, H_e and Δt are conservatively estimated to be 350 m and ¼ day, respectively. The term T_b is calculated using ERAI data. Prescribing T_b to 300 K, as done in Li and Carbone (2012), does not significantly alter the boundary layer divergence solution shown in Fig. 12.

Instead of concentrating on the amplitude of individual dipoles of the LSST and divergence, we choose to focus on the net effect of the LSST, and thus the net divergence, over a broad region as recommended by Carbone and Li (2015). The relevant region of this study is the near-off-equatorial area of the western Indian Ocean where oceanic ER waves are known to reemerge in SSH and SST anomalies. Figure 12 shows the 20–200-day bandpass-filtered ERAI divergence and OLR anomalies averaged over the 2°–6° latitude bands and

50°–65°E longitude band. Divergence is averaged over the 1000–850-hPa boundary layer. The averaging longitudes capture the overlapping region of the $|\nabla \mathrm{SST}|$ maximum and OLR minimum (see Fig. 11) in the western Indian Ocean. The ERAI convergence anomaly peaks near lag +6 days at $3.2 \times 10^{-7}\,\mathrm{s}^{-1}$. Maximum boundary layer convergence occurs ~5 days prior to the OLR minimum. The boundary layer divergence anomalies calculated from Eqs. (1) and (2) are averaged over the same domain and shown in Fig. 12. The solutions to Eqs. (1) and (2) are nearly identical in their phasing and amplitude. This might be expected given both equations are proportional to the LSST. The equations diagnose peak convergence anomalies of $1.5 \times 10^{-7}\,\mathrm{s}^{-1}$ near lags +7 and +8 days. The diagnosed boundary layer convergence peaks 3–4 days prior to the OLR minimum and only slightly lags the observed convergence. At lag +6 days, the convergence diagnosed from the equations accounts for ~45% of the observed convergence.

The present study reinforces the results of Webber et al. (2010) by showing that independent methods of compositing ER waves produce similar results; namely, ER waves in the western Indian Ocean precede MJO convective onset. While previous studies hypothesized that MJO convective onset forced by ER waves is primarily achieved through enhanced surface fluxes, these results show that enhanced surface fluxes are likely a consequence of convection. Instead, these findings suggest that ER waves modulate the SST field and preferentially drive boundary layer convergence in the western Indian Ocean, triggering MJO convection. The next section examines to what degree ER waves assist the organization of boundary layer moisture that is supportive of MJO convection.

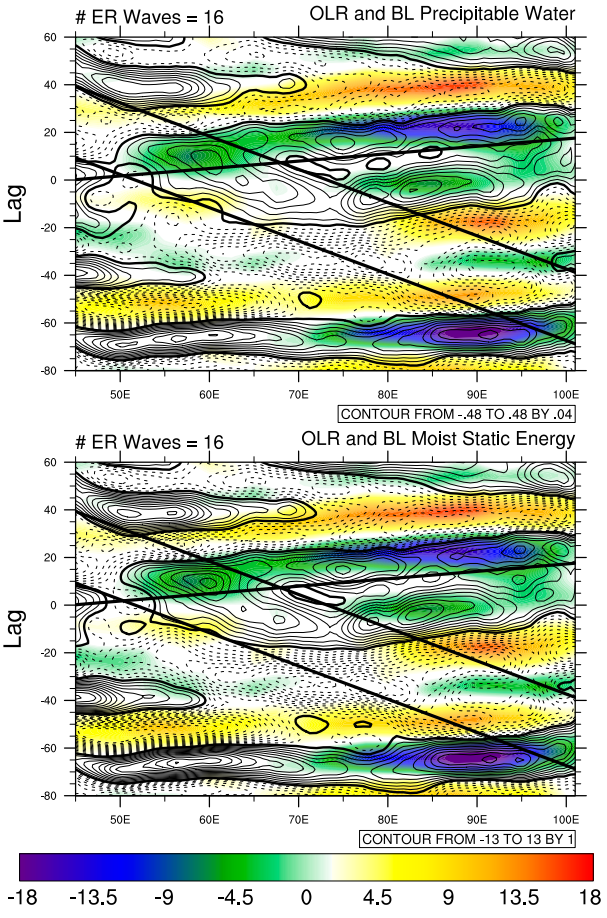

FIG. 13. As in Fig. 9, but for (top) OLR (color; $\mathrm{W\,m^{-2}}$) and boundary layer total precipitable water (contours; mm) anomalies and (bottom) OLR (color; $\mathrm{W\,m^{-2}}$) and boundary layer vertically integrated moist static energy (contours; $\mathrm{W\,day\,m^{-2}}$) anomalies. Boundary layer precipitable water contours range from −0.48 to +0.48 mm with a 0.04-mm contour interval. Boundary layer moist static energy contours range from $-13\,\mathrm{W\,day\,m^{-2}}$ to $+13\,\mathrm{W\,day\,m^{-2}}$ with a $1\,\mathrm{W\,day\,m^{-2}}$ contour interval.

4. Boundary layer moisture budget

The process by which ER waves assist the local increase of boundary layer total precipitable water (TPW) prior to the initiation of the MJO in the western Indian Ocean is the focus of this section. Although free-tropospheric moisture is important for tropical deep convection (e.g., Brown and Zhang 1997; Bretherton et al. 2004), this section focuses on the shallow moistening signal observed to lead MJO deep convection and support shallow convection that assists in the moistening of the overlying free troposphere (e.g., Kemball-Cook and Weare 2001; Sperber 2003; Kiladis et al. 2005; Benedict and Randall 2007; Seo and Kumar 2008; Hsu and Li 2012; Zhao et al. 2013; Ruppert and Johnson 2015). Figure 13 (top) shows the composite of 20–200-day bandpass-filtered OLR and boundary layer (1000–850 hPa) TPW anomalies. Coincident with the trajectory of the ER wave, a tongue of anomalously increased TPW begins near 74°E at lag −10 days and propagates westward. The TPW anomaly increases to 0.2 mm upon reaching 60°E at lag +5 days. The increase of boundary layer TPW prior to peak MJO convection in the western Indian Ocean is consistent with previously observed MJO behavior mentioned at the beginning of the section. The phase relationship of boundary layer TPW and OLR anomalies appears consistent across the MJO life cycle in the Indian Ocean as positive boundary layer TPW anomalies propagate eastward with MJO convection. Boundary layer TPW also increases rapidly in the central Indian Ocean near 78°E and lag −10 days and propagates eastward at $4\,\mathrm{m\,s^{-1}}$. This suggests that intraseasonal convection might also be initialized in the central Indian Ocean by ER

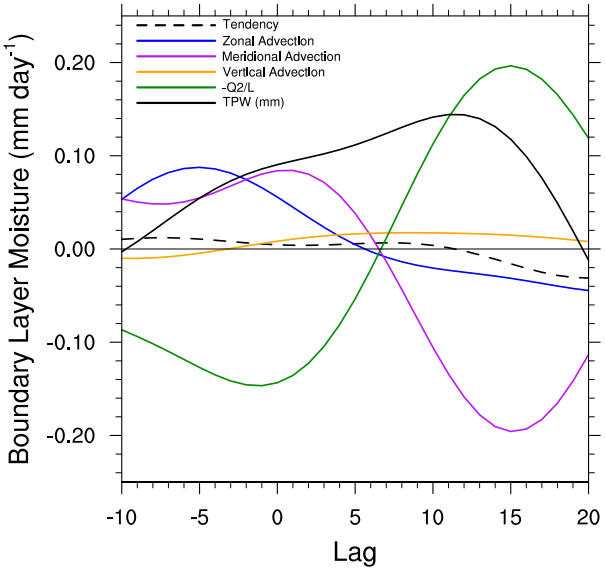

FIG. 14. Composites of 20–200-day bandpass-filtered boundary layer moisture tendency (dashed black; mm day^{-1}), zonal moisture advection (blue; mm day^{-1}), meridional moisture advection (purple; mm day^{-1}), vertical moisture advection (yellow; mm day^{-1}), apparent moisture sink (green; mm day^{-1}), and boundary layer total precipitable water (black; mm) anomalies averaged over the latitude bands 2°–6°S and 2°–6°N and longitudes 50°–65°E. Composites are based on 16 ER wave events and shown for lags from −10 to +20 days.

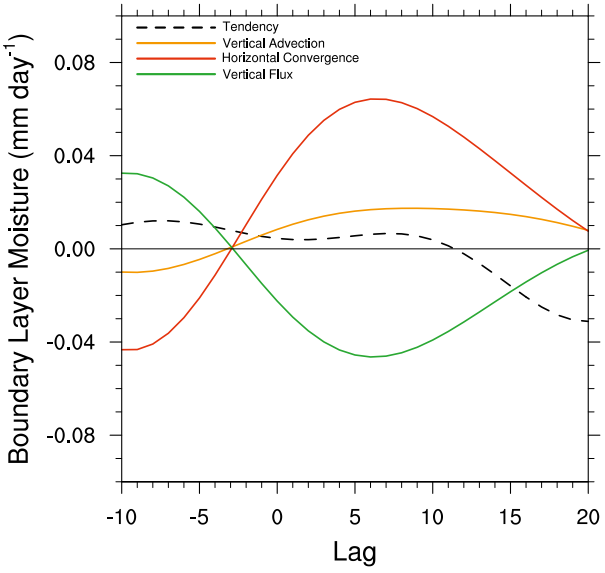

FIG. 15. As in Fig. 14, but for the boundary layer moisture tendency (black; mm day^{-1}), vertical moisture advection (yellow; mm day^{-1}), horizontal moisture convergence (red; mm day^{-1}), and vertical moisture flux (green; mm day^{-1}) anomalies.

waves, as suggested by Shinoda et al. (2013). However, such events do not appear to be as robust as those forced in the western Indian Ocean using the present ER wave index and are reserved for future analysis. Figure 13 (bottom) shows the 20–200-day bandpass-filtered vertically integrated boundary layer moist static energy anomalies. The moist static energy anomalies largely reflect the patterns of the boundary layer TPW. This suggests that boundary layer moisture largely controls boundary layer moist static energy in the composites, similar to what might be expected in the free troposphere under the weak temperature gradient approximation (Sobel and Bretherton 2000; Sobel et al. 2001).

To investigate the processes responsible for the local increase of boundary layer TPW in the western Indian Ocean, the boundary layer moisture budget is examined. The intraseasonal and vertically integrated boundary layer moisture budget may be expressed as follows:

$$\left[\frac{\partial q}{\partial t}\right]' = -[\mathbf{U}\cdot\nabla q]' - \left[\omega\frac{\partial q}{\partial p}\right]' - \left[\frac{Q_2}{L}\right]', \qquad (3)$$

where

$$-\left[\omega\frac{\partial q}{\partial p}\right]' = [q\nabla\cdot\mathbf{U}]' - \left[\frac{\partial(\omega q)}{\partial p}\right]', \qquad (4)$$

similar to the analysis of boundary layer moisture by Hsu and Li (2012). Here, square brackets indicate the mass-weighted vertical integral from 1000 to 850 hPa, and primes indicate 20–200-day bandpass-filtered anomalies. In this equation q is the specific humidity, $\mathbf{U}$ is the horizontal wind, ω is the vertical wind, Q_2 is the apparent moisture sink, and L is the latent heat of vaporization. The term on the LHS of Eq. (3) is the moisture tendency. The first and second terms on the RHS of Eq. (3) are the horizontal and vertical moisture advection, respectively. The vertical moisture advection may also be written as the sum of the horizontal moisture convergence and vertical moisture flux convergence as indicated by Eq. (4). The third term on the RHS of Eq. (3) is the moisture tendency resulting from the apparent moisture sink. This term Q_2/L is calculated as the residual of the total derivative of q.

In this budget, we are primarily concerned with the moisture tendency resulting from the horizontal convergence of moisture. In the previous section, horizontal convergence owing to negative LSST was shown to be a leading contributor to the intraseasonal convergence observed in the western Indian Ocean that precedes MJO deep convection. In this section we determine if horizontal convergence of moisture is likewise important to the net buildup of moisture in the western Indian Ocean. Figure 14 shows the composited boundary layer moisture budget terms averaged over the same domain as the divergence anomalies shown in Fig. 12. The moisture tendency (dashed black line) is positive from

lag −10 to +11 days and is associated with increasing MJO convective activity (see Fig. 11). At lag +11 days, the moisture tendency becomes negative, and negative OLR anomalies over the domain begin to weaken. The moisture tendency is marginally positive during the buildup phases with local maxima of approximately $0.012\,\mathrm{mm\,day^{-1}}$ at lag −7 and $0.007\,\mathrm{mm\,day^{-1}}$ at lag +7 days. Because the moisture tendency in this region is relatively weak, even small contributors to the tendency are important. During lag −10 to +11 days, the boundary layer TPW anomalies (solid black line) over the western Indian Ocean gradually increases from near zero at lag −10 days to 0.14 mm at lag +11 days. The boundary layer TPW anomaly becomes negative at lag +19 days.

Prior to lag +5 days, horizontal advection is positive (Fig. 14). The apparent moisture sink Q_2/L largely offsets the boundary layer moistening resulting from horizontal advection during this period. The apparent moisture sink is strongly correlated with surface latent heat fluxes (see Fig. 9). By lag +7 days, horizontal advection and the apparent moisture sink change sign. While zonal advection contributes to a moderate decrease in moisture from lags +6 to +20 days, meridional advection is strongly negative, eventually reaching $-0.2\,\mathrm{mm\,day^{-1}}$ at lag +15 days. Moistening by the apparent moisture sink largely offsets the drying by meridional advection after lag +6 days.

Vertical advection switches sign at lag −3 days from a negative to a positive tendency (Fig. 14). Figure 15 shows the moisture tendency, vertical moisture advection, and components of the vertical moisture advection (horizontal moisture convergence and vertical moisture flux). The sign change of vertical moisture advection is coincident with the change in sign of horizontal moisture convergence and the vertical flux. At this same time, horizontal convergence in the boundary layer begins (see Fig. 12). Between lag −3 days and lag +20 days, vertical moisture advection is positive with values near $0.01\,\mathrm{mm\,day^{-1}}$, comparable to the total moisture tendency. The leading contributor to vertical advection during this period is horizontal moisture convergence with a maximum of $0.06\,\mathrm{mm\,day^{-1}}$ at lag +6 days. At the same time, the vertical moisture flux is negative, reducing the net effect of horizontal moisture convergence on vertical moisture advection. Between lags −3 to +20 days, horizontal moisture convergence in the boundary layer exceeds the amount of moisture fluxed out of (or dry air fluxed into) the boundary layer. Horizontal moisture convergence almost completely results from convergence anomalies (<200 days) operating on the mean moisture gradient (not shown). This process, as well as the anomalous moistening by the apparent moisture sink, counters the drying effects of horizontal advection and result in net moistening of the boundary layer in the western Indian Ocean. Because the SST field is a critical contributor to the horizontal convergence anomalies in the boundary layer, it is important to the horizontal convergence of moisture that assists in moistening the boundary layer.

5. Discussion and conclusions

The arrival of downwelling ER waves in the western Indian Ocean is synchronous with the initiation of certain MJO events. The ER waves are partly forced by the active phase of the MJO that occurs in the eastern Indian Ocean ~75 days earlier, suggesting long lead times for predictability of the ensuing MJO event. Downwelling ER waves permit an increase in SST and enhancement of SST gradients in the western Indian Ocean. Enhanced SST gradients drive anomalous circulations in the boundary layer, modifying the low-level flow field. ER waves are hypothesized to initiate MJO convection via forcing of boundary layer convergence that is estimated using the Laplacian of the SST field. Up to 45% of the anomalous boundary layer convergence in the western Indian Ocean is explained by the anomalous SST structure that results from downwelling ER waves. The diagnosed boundary layer convergence maximum from Eqs. (1) and (2) precedes the convective maximum by several days and is hypothesized to be critical to the initiation of MJO deep convection. The effect of diabatic heating on boundary layer convergence likely contributes a significant amount to the remainder (55%) of the intraseasonal boundary layer convergence but is not quantified in this study.

MJO deep convection is augmented by the horizontal convergence of boundary layer moisture that is, again, partly forced by the SST field. The warm SST anomalies in the western Indian Ocean that develop in association with downwelling ER waves are also accompanied by enhanced latent heat fluxes. During MJO convective onset, latent heat flux anomalies are ~13%–20% of the anomalous precipitation magnitude. Because latent heat flux anomalies slightly lag MJO convection, they help maintain convection but do not appear responsible for its initiation. The effects of ER waves are predominantly confined to the western Indian Ocean, and mechanisms of MJO eastward propagation likely rely on processes independent of ER waves.

DeMott et al. (2016) analyzed the direct contribution by SST to surface heat fluxes during boreal winter using ERAI data. In their results, positive heat flux anomalies directly resulting from SST anomalies were in phase with enhanced precipitation during MJO initiation in

the western Indian Ocean, indicating an important role for surface flux anomalies not directly resulting from wind speed variability. The unique phase alignment of SST and MJO convective anomalies in the western Indian Ocean observed in Fig. 7 and the investigation of DeMott et al. (2016) suggest that the western Indian Ocean is uniquely poised to encourage the development and amplification of intraseasonal convection.

The process of low-level moistening by ER waves fits with observed life cycles and vertical structures of the MJO. For example, many observational studies show that the life cycle of the MJO begins with low-level convergence and moistening of the boundary layer that subsequently leads to shallow convection and moistening of the midtroposphere followed by deep convection (e.g., Kemball-Cook and Weare 2001; Kiladis et al. 2005; Benedict and Randall 2007; Seo and Kumar 2008; Ruppert and Johnson 2015). Low-level moistening has also been suggested as the most important feature for determining MJO deep convection (Agudelo et al. 2006). Previous observational studies have shown that the variability of SST associated with the MJO results from net surface flux forcing controlled to a large degree by the atmosphere (e.g., Hendon and Glick 1997; Lau and Sui 1997; Shinoda et al. 1998; Jones et al. 1998; Flatau et al. 1997). Typically, SST anomalies maximize just prior to MJO convection as a result of decreased surface evaporation and increased insolation. After convection initiates, SST anomalies rapidly cool (Shinoda et al. 1998; Zhang and McPhaden 2000; Moum et al. 2014; de Szoeke et al. 2015). The ER index identifies a class of MJO events that deviate from this relationship during convective onset. For these MJO events, subsurface oceanic processes and/or horizontal advection maintain warm SST anomalies in the presence of enhanced evaporation and reduced insolation, thus aligning the phases of warm SST and enhanced convection anomalies.

Some features of MJO convective onset are unresolved in this analysis. While the peak of anomalous horizontal convergence leads the peak convergence diagnosed from Eqs. (1) and (2) by just 1 day, convergence in the boundary layer begins ~4 days before the diagnosed convergence begins. This is likely due to the diabatic effects of shallow and nonprecipitating convection, which the diagnostic boundary layer divergence equations utilized in this study do not consider. Additionally, boundary layer convergence associated with a reduction of the geopotential height at the boundary layer top, as can occur with a passing Kelvin wave, is omitted in the diagnosis of boundary layer convergence. Another open question is how and if boundary layer winds forced by the SST gradient are important to surface latent heat fluxes. When averaged over the western Indian Ocean, the horizontal winds diagnosed from the SST gradient are very weak. This suggests that the increase in total wind speed responsible for forcing increased latent heat flux anomalies is mostly a result of convective heating anomalies and not SST gradient anomalies. The influence of SST gradient anomalies on boundary layer winds may vary when examining MJO events in different locations of the tropics.

To further investigate the role of the SST field in determining MJO convective onset, the authors plan to use the U.S. Navy's Coupled Ocean–Atmosphere Mesoscale Prediction System (COAMPS) model. In COAMPS, reflected ER waves in the Indian Ocean can be eliminated by removing the eastern landmass. The hypothesis presented in this study is supported if the amplitude of intraseasonal convective activity is significantly weakened by the removal of reflected ER waves. If intraseasonal convective activity and MJO initiation are unaffected, the mechanism of MJO initiation by ER waves must be reconsidered.

This hypothesis does not attempt to explain the initialization of all MJO events but rather those in a specific region of the Indian Ocean during periods when robust downwelling ER waves are present. In the study of Matthews (2008), an identifiable mechanism was not found to precede primary MJO events. The mechanisms proposed herein are likely too limited geographically and seasonally to explain the initiation of a majority of MJO events. Moreover, we suspect that the impact of ER waves is most manifest when the atmosphere is susceptible to weak excitation, and alternative large-scale forcing mechanisms are absent. Future work aims to examine the sensitivity of ER wave forcing to variations in the Indian Ocean basic state to better understand the boreal summer bias of strong ER wave events. Also, we intend to explore the effects of ER waves on MJO events that initiate in the central Indian Ocean, where SST variations associated with ER waves are generally weaker. For example, downwelling ER waves have been suggested as being responsible for the initiation of the MJO in the central Indian Ocean in March of 2012 (see last boreal winter event in Table 2) at the end of the CINDY/DYNAMO field campaign (Shinoda et al. 2013).

Acknowledgments. We thank Simon P. de Szoeke and two anonymous reviewers, whose thoughtful comments improved this work. This research was sponsored by the U.S. Naval Research Laboratory 6.2 project, "The Madden–Julian Oscillation: Key to Coupled Extended-Range Predictability" (BE0435-003-T022-14), and the U.S. Office of Naval Research PISTON (73-4347-27-5) and NASCar (73-4347-34-5) projects.

REFERENCES

Agudelo, P. A., J. A. Curry, C. D. Hoyos, and P. J. Webster, 2006: Transition between suppressed and active phases of intraseasonal oscillations in the Indo-Pacific warm pool. *J. Climate*, **19**, 5519–5530, doi:10.1175/JCLI3924.1.

Araligidad, N. M., and E. D. Maloney, 2008: Wind-driven latent heat flux and the intraseasonal oscillation. *Geophys. Res. Lett.*, **35**, L04815, doi:10.1029/2007GL032746.

Back, L. E., and C. S. Bretherton, 2009: On the relationship between SST gradients, boundary layer winds, and convergence over the tropical oceans. *J. Climate*, **22**, 4182–4196, doi:10.1175/2009JCLI2392.1.

Battisti, D. S., 1988: Dynamics and thermodynamics of a warming event in a coupled tropical atmosphere ocean model. *J. Atmos. Sci.*, **45**, 2889–2919, doi:10.1175/1520-0469(1988)045<2889:DATOAW>2.0.CO;2.

Benedict, J. J., and D. A. Randall, 2007: Observed characteristics of the MJO relative to maximum rainfall. *J. Atmos. Sci.*, **64**, 2332–2354, doi:10.1175/JAS3968.1.

Bretherton, C. S., M. E. Peters, and L. E. Back, 2004: Relationships between water vapor path and precipitation over the tropical oceans. *J. Climate*, **17**, 1517–1528, doi:10.1175/1520-0442(2004)017<1517:RBWVPA>2.0.CO;2.

Brown, R. G., and C. Zhang, 1997: Variability of midtropospheric moisture and its effect on cloud-top height distribution during TOGA COARE. *J. Atmos. Sci.*, **54**, 2760–2774, doi:10.1175/1520-0469(1997)054<2760:VOMMAI>2.0.CO;2.

Carbone, R. E., and Y. Li, 2015: Tropical oceanic rainfall and sea surface temperature structure: Parsing causation from correlation in the MJO. *J. Atmos. Sci.*, **72**, 2703–2718, doi:10.1175/JAS-D-14-0226.1.

Chelton, D. B., R. A. DeSzoeke, M. G. Schlax, K. El Naggar, and N. Siwertz, 1998: Geographical variability of the first baroclinic Rossby radius of deformation. *J. Phys. Oceanogr.*, **28**, 433–460, doi:10.1175/1520-0485(1998)028<0433:GVOTFB>2.0.CO;2.

Dee, D. P., and Coauthors, 2011: The ERA-Interim reanalysis: Configuration and performance of the data assimilation system. *Quart. J. Roy. Meteor. Soc.*, **137**, 553–597, doi:10.1002/qj.828.

Delcroix, T., J. Picaut, and G. Eldin, 1991: Equatorial Kelvin and Rossby waves evidence in the Pacific Ocean through Geosat sea level and surface current anomalies. *J. Geophys. Res.*, **96**, 3249–3262, doi:10.1029/90JC01758.

DeMott, C. A., N. P. Klingman, and S. J. Woolnough, 2015: Atmosphere–ocean coupled processes in the Madden-Julian oscillation. *Rev. Geophys.*, **53**, 1099–1154, doi:10.1002/2014RG000478.

——, J. J. Benedict, N. P. Klingaman, S. J. Woolnough, and D. A. Randall, 2016: Diagnosing ocean feedbacks to the MJO: SST-modulated surface fluxes and the moist static energy budget. *J. Geophys. Res. Atmos.*, **121**, 8350–8373, doi:10.1002/2016JD025098.

de Szoeke, S., J. Edson, J. Marion, C. Fairall, and L. Bariteau, 2015: The MJO and air–sea interaction in TOGA COARE and DYNAMO. *J. Climate*, **28**, 597–622, doi:10.1175/JCLI-D-14-00477.1.

Enfield, D., 1987: The intraseasonal oscillation in eastern Pacific sea levels: How is it forced? *J. Phys. Oceanogr.*, **17**, 1860–1876, doi:10.1175/1520-0485(1987)017<1860:TIOIEP>2.0.CO;2.

Flatau, M., P. J. Flatau, P. Phoebus, and P. P. Niiler, 1997: The feedback between equatorial convection and local radiative and evaporative processes: The implications for intraseasonal oscillations. *J. Atmos. Sci.*, **54**, 2373–2386, doi:10.1175/1520-0469(1997)054<2373:TFBECA>2.0.CO;2.

Gent, P. R., K. O'Neill, and M. A. Cane, 1983: A model of the semiannual oscillation in the equatorial Indian Ocean. *J. Phys. Oceanogr.*, **13**, 2148–2160, doi:10.1175/1520-0485(1983)013<2148:AMOTSO>2.0.CO;2.

Gottschalck, J., P. Roundy, C. Schreck III, A. Vintzileos, and C. Zhang, 2013: Large-scale atmospheric and oceanic conditions during the 2011–12 DYNAMO field campaign. *Mon. Wea. Rev.*, **141**, 4173–4196, doi:10.1175/MWR-D-13-00022.1.

Gribble-Verhagen, L., and P. E. Roundy, 2010: Analysis of apparent coupling between an oceanic Kelvin wave and atmospheric convection during the winter of 1986/87. *J. Climate*, **23**, 6352–6364, doi:10.1175/2010JCLI3790.1.

Gutzler, D. S., G. N. Kiladis, O. A. Meehi, K. M. Weickmann, and M. Wheeler, 1994: The global climate of December 1992–February 1993. Part II: Large-scale variability across the tropical western Pacific during TOGA COARE. *J. Climate*, **7**, 1606–1622, doi:10.1175/1520-0442(1994)007<1606:TGCODP>2.0.CO;2.

Han, W., J. P. McCreary, D. L. T. Anderson, and A. J. Mariano, 1999: Dynamics of the eastern surface jets in the equatorial Indian Ocean. *J. Phys. Oceanogr.*, **29**, 2191–2209, doi:10.1175/1520-0485(1999)029<2191:DOTESJ>2.0.CO;2.

——, D. M. Lawrence, and P. J. Webster, 2001: Dynamical response of equatorial Indian Ocean to intraseasonal winds: Zonal flow. *Geophys. Res. Lett.*, **28**, 4215–4218, doi:10.1029/2001GL013701.

Hendon, H. H., and M. L. Salby, 1994: The life cycle of the Madden–Julian oscillation. *J. Atmos. Sci.*, **51**, 2225–2237, doi:10.1175/1520-0469(1994)051<2225:TLCOTM>2.0.CO;2.

——, and J. Glick, 1997: Intraseasonal air–sea interaction in the tropical Indian and Pacific Oceans. *J. Climate*, **10**, 647–661, doi:10.1175/1520-0442(1997)010<0647:IASIIT>2.0.CO;2.

——, B. Liebmann, and J. Glick, 1998: Oceanic Kelvin waves and the Madden–Julian oscillation. *J. Atmos. Sci.*, **55**, 88–101, doi:10.1175/1520-0469(1998)055<0088:OKWATM>2.0.CO;2.

Hermes, J. C., and C. J. C. Reason, 2008: Annual cycle of the south Indian Ocean (Seychelles–Chagos) thermocline ridge in a regional ocean model. *J. Geophys. Res.*, **113**, C04035, doi:10.1029/2007JC004363.

Hsu, P., and T. Li, 2012: Role of the boundary layer moisture asymmetry in causing the eastward propagation of the Madden–Julian oscillation. *J. Climate*, **25**, 4914–4931, doi:10.1175/JCLI-D-11-00310.1.

Huffman, G. J., and Coauthors, 2007: The TRMM Multisatellite Precipitation Analysis (TMPA): Quasi-global, multiyear, combined-sensor precipitation estimates at fine scales. *J. Hydrometeor.*, **8**, 38–55, doi:10.1175/JHM560.1.

Iskandar, I., and M. J. McPhaden, 2011: Dynamics of wind-forced intraseasonal zonal current variation in the equatorial Indian Ocean. *J. Geophys. Res.*, **116**, C06019, doi:10.1029/2010JC006864.

Jensen, T. G., 1993: Equatorial variability and resonance in a wind-driven Indian Ocean model. *J. Geophys. Res.*, **98**, 22 533–22 552, doi:10.1029/93JC02565.

——, T. Shinoda, S. Chen, and M. Flatau, 2015: Ocean response to CINDY/DYNAMO MJOs in air–sea-coupled COAMPS. *J. Meteor. Soc. Japan*, **93A**, 157–178, doi:10.2151/jmsj.2015-049.

Jones, C., D. E. Waliser, and C. Gautier, 1998: The influence of the Madden–Julian oscillation on ocean surface heat fluxes and sea surface temperature. *J. Climate*, **11**, 1057–1072, doi:10.1175/1520-0442(1998)011<1057:TIOTMJ>2.0.CO;2.

Kemball-Cook, S. R., and B. C. Weare, 2001: The onset of convection in the Madden–Julian oscillation. *J. Climate*, **14**, 780–793, doi:10.1175/1520-0442(2001)014<0780:TOOCIT>2.0.CO;2.

Kessler, W. S., and R. Kleeman, 2000: Rectification of the Madden–Julian oscillation into the ENSO cycle. *J. Climate*, **13**, 3560–3575, doi:10.1175/1520-0442(2000)013<3560:ROTMJO>2.0.CO;2.

——, M. J. McPhaden, and K. M. Wieckmann, 1995: Forcing of intraseasonal Kelvin waves in the equatorial Pacific. *J. Geophys. Res.*, **100**, 10 613–10 631, doi:10.1029/95JC00382.

Kiladis, G. N., K. H. Straub, and P. T. Haertel, 2005: Zonal and vertical structure of the Madden–Julian oscillation. *J. Atmos. Sci.*, **62**, 2790–2809, doi:10.1175/JAS3520.1.

Kumar, B. P., J. Vialard, M. Lengaigne, V. S. N. Murt, and M. J. McPhaden, 2012: TropFlux: Air–sea fluxes for the global tropical oceans—Description and evaluation. *Climate Dyn.*, **38**, 1521–1543, doi:10.1007/s00382-011-1115-0.

Lau, K.-M., and C.-H. Sui, 1997: Mechanisms of short-term sea surface temperature regulation: Observations during TOGA COARE. *J. Climate*, **10**, 465–472, doi:10.1175/1520-0442(1997)010<0465:MOSTSS>2.0.CO;2.

Li, Y., and R. E. Carbone, 2012: Excitation of rainfall over the tropical western Pacific. *J. Atmos. Sci.*, **69**, 2983–2994, doi:10.1175/JAS-D-11-0245.1.

Liebmann, B., and C. A. Smith, 1996: Description of a complete (interpolated) outgoing longwave radiation dataset. *Bull. Amer. Meteor. Soc.*, **77**, 1275–1277.

Lindzen, R. S., and S. Nigam, 1987: On the role of sea surface temperature gradients in forcing low-level wind and convergence in the tropics. *J. Atmos. Sci.*, **44**, 2418–2436, doi:10.1175/1520-0469(1987)044<2418:OTROSS>2.0.CO;2.

Madden, R. A., and P. R. Julian, 1972: Description of global-scale circulation cells in the tropics with a 40–50 day period. *J. Atmos. Sci.*, **29**, 1109–1123, doi:10.1175/1520-0469(1972)029<1109:DOGSCC>2.0.CO;2.

Maloney, E. D., and D. L. Hartmann, 1998: Frictional moisture convergence in a composite life cycle of the Madden–Julian oscillation. *J. Climate*, **11**, 2387–2403, doi:10.1175/1520-0442(1998)011<2387:FMCIAC>2.0.CO;2.

Matsuno, T., 1966: Quasi-geostrophic motions in the equatorial area. *J. Meteor. Soc. Japan*, **44**, 25–43.

Matthews, A. J., 2008: Primary and successive events in the Madden–Julian oscillation. *Quart. J. Roy. Meteor. Soc.*, **134**, 439–453, doi:10.1002/qj.224.

McPhaden, M. J., 1999: Genesis and evolution of the 1997–98 El Niño. *Science*, **283**, 950–954, doi:10.1126/science.283.5404.950.

Moum, J. N., and Coauthors, 2014: Air–sea interaction from westerly wind bursts during the November 2011 MJO in the Indian Ocean. *Bull. Amer. Meteor. Soc.*, **95**, 1185–1199, doi:10.1175/BAMS-D-12-00225.1.

O'Brien, J. J., and H. E. Hurlburt, 1974: An equatorial jet in the Indian Ocean, theory. *Science*, **184**, 1075–1077, doi:10.1126/science.184.4141.1075.

Oliver, E. C. J., and K. R. Thompson, 2010: Madden-Julian oscillation and sea level: Local and remote forcing. *J. Geophys. Res.*, **115**, C01003, doi:10.1029/2009JC005337.

Pascual, A., Y. Faugere, G. Larnicol, and P. Le Traon, 2006: Improved description of the ocean mesoscale variability by combining four satellite altimeters. *Geophys. Res. Lett.*, **33**, L02611, doi:10.1029/2005GL024633.

Reynolds, R. W., T. M. Smith, C. Liu, D. B. Chelton, K. S. Casey, and M. G. Schlax, 2007: Daily high-resolution-blended analyses for sea surface temperature. *J. Climate*, **20**, 5473–5496, doi:10.1175/2007JCLI1824.1.

Riley Dellaripa, E. M., and E. D. Maloney, 2015: Analysis of MJO wind-flux feedbacks in the Indian Ocean using RAMA buoy observations. *J. Meteor. Soc. Japan*, **93A**, 1–20, doi:10.2151/jmsj.2015-021.

Roundy, P. E., and G. N. Kiladis, 2006: Observed relationships between oceanic Kelvin waves and atmospheric forcing. *J. Climate*, **19**, 5253–5272, doi:10.1175/JCLI3893.1.

Ruppert, J. H., and R. H. Johnson, 2015: Diurnally modulated cumulus moistening in the preonset stage of the Madden–Julian oscillation during DYNAMO. *J. Atmos. Sci.*, **72**, 1622–1647, doi:10.1175/JAS-D-14-0218.1.

Schott, F., and D. Quadfasel, 1983: Currents and transports of the monsoon current south of Sri Lanka. *Prog. Oceanogr.*, **12**, 357–381, doi:10.1016/0079-6611(83)90014-9.

Seiki, A., M. Katsumata, T. Horii, T. Hasegawa, K. J. Richards, K. Yoneyama, and R. Shirooka, 2013: Abrupt cooling associated with the oceanic Rossby wave and lateral advection during CINDY2011. *J. Geophys. Res. Oceans*, **118**, 5523–5535, doi:10.1002/jgrc.20381.

Seo, K.-H., and A. Kumar, 2008: The onset and life span of the Madden–Julian oscillation. *Theor. Appl. Climatol.*, **94**, 13–24, doi:10.1007/s00704-007-0340-2.

Shinoda, T., and H. H. Hendon, 2002: Rectified wind forcing and latent heat flux produced by the Madden–Julian oscillation. *J. Climate*, **15**, 3500–3508, doi:10.1175/1520-0442(2002)015<3500:RWFALH>2.0.CO;2.

——, ——, and J. Glick, 1998: Intraseasonal variability of surface fluxes and sea surface temperature in the tropical western Pacific and Indian Oceans. *J. Climate*, **11**, 1685–1702, doi:10.1175/1520-0442(1998)011<1685:IVOSFA>2.0.CO;2.

——, G. N. Kiladis, and P. E. Roundy, 2009: Statistical representation of equatorial waves and tropical instability waves in the equatorial Pacific Ocean. *Atmos. Res.*, **94**, 37–44, doi:10.1016/j.atmosres.2008.06.002.

——, T. G. Jensen, M. Flatau, S. Chen, W. Han, and C. Wang, 2013: Large-scale oceanic variability associated with the Madden-Julian oscillation during the CINDY/DYNAMO field campaign from satellite observations. *Remote Sens.*, **5**, 2072–2092, doi:10.3390/rs5052072.

——, W. Han, T. G. Jensen, L. Zamudio, E. J. Metzger, and R.-C. Lien, 2016: Impact of the Madden–Julian oscillation on the Indonesian Throughflow in Makassar Strait during the CINDY/DYNAMO field campaign. *J. Climate*, **29**, 6085–6108, doi:10.1175/JCLI-D-15-0711.1.

Sobel, A. H., and C. S. Bretherton, 2000: Modeling tropical precipitation in a single column. *J. Climate*, **13**, 4378–4392, doi:10.1175/1520-0442(2000)013<4378:MTPIAS>2.0.CO;2.

——, J. Nilsson, and L. M. Polvani, 2001: The weak temperature gradient approximation and balanced tropical moisture waves. *J. Atmos. Sci.*, **58**, 3650–3655, doi:10.1175/1520-0469(2001)058<3650:TWTGAA>2.0.CO;2.

Sperber, K. R., 2003: Propagation and the vertical structure of the Madden–Julian oscillation. *Mon. Wea. Rev.*, **131**, 3018–3037, doi:10.1175/1520-0493(2003)131<3018:PATVSO>2.0.CO;2.

——, J. M. Slingo, P. M. Inness, and W. K.-M. Lau, 1997: On the maintenance and initiation of the intraseasonal oscillation in the NCEP/NCAR reanalysis and in the GLA and IKMO AMIP simulations. *Climate Dyn.*, **13**, 769–795, doi:10.1007/s003820050197.

Wang, B., and T. Li, 1993: A simple tropical atmosphere model of relevance to short-term climate variations. *J. Atmos. Sci.*, **50**, 260–284, doi:10.1175/1520-0469(1993)050<0260:ASTAMO>2.0.CO;2.

——, P. Webster, K. Kikuchi, T. Yasunari, and Y. Qi, 2006: Boreal summer quasi-monthly oscillation in the global tropics. *Climate Dyn.*, **27**, 661–675, doi:10.1007/s00382-006-0163-3.

Webber, B. G. M., A. J. Matthews, and K. J. Heywood, 2010: A dynamical ocean feedback mechanism for the Madden–Julian oscillation. *Quart. J. Roy. Meteor. Soc.*, **136**, 740–754, doi:10.1002/qj.604.

——, ——, ——, and D. P. Stevens, 2012a: Ocean Rossby wave as a triggering mechanism for primary Madden–Julian events. *Quart. J. Roy. Meteor. Soc.*, **138**, 514–527, doi:10.1002/qj.936.

——, D. P. Stevens, A. J. Matthews, and K. J. Heywood, 2012b: Dynamical ocean forcing of the Madden–Julian oscillation at lead times of up to five months. *J. Climate*, **25**, 2824–2842, doi:10.1175/JCLI-D-11-00268.1.

——, A. J. Matthews, K. J. Heywood, J. Kaiser, and S. Schmidtko, 2014: Seaglider observations of equatorial Indian Ocean Rossby waves associated with the Madden-Julian oscillation. *J. Geophys. Res. Oceans*, **119**, 3714–3731, doi:10.1002/2013JC009657.

Wheeler, M. C., and G. N. Kiladis, 1999: Convectively coupled equatorial waves: Analysis of clouds and temperature in the wavenumber–frequency domain. *J. Atmos. Sci.*, **56**, 374–399, doi:10.1175/1520-0469(1999)056<0374:CCEWAO>2.0.CO;2.

——, and H. H. Hendon, 2004: An all-season real-time multivariate MJO index: Development of an index for monitoring and prediction. *Mon. Wea. Rev.*, **132**, 1917–1932, doi:10.1175/1520-0493(2004)132<1917:AARMMI>2.0.CO;2.

Woolnough, S. J., J. M. Slingo, and B. J. Hoskins, 2000: The relationship between convection and sea surface temperature on intraseasonal timescales. *J. Climate*, **13**, 2086–2104, doi:10.1175/1520-0442(2000)013<2086:TRBCAS>2.0.CO;2.

Wyrtki, K., 1973: An equatorial jet in the Indian Ocean. *Science*, **181**, 262–264, doi:10.1126/science.181.4096.262.

Xie, S. P., H. Annamalai, F. A. Schott, and J. P. McCreary, 2002: Structure and mechanisms of south Indian Ocean climate variability. *J. Climate*, **15**, 864–878, doi:10.1175/1520-0442(2002)015<0864:SAMOSI>2.0.CO;2.

Zhang, C., and M. McPhaden, 2000: Intraseasonal surface cooling in the equatorial western Pacific. *J. Climate*, **13**, 2261–2276, doi:10.1175/1520-0442(2000)013<2261:ISCITE>2.0.CO;2.

Zhao, C., T. Li, and T. Zhou, 2013: Precursor signals and processes associated with MJO initiation over the tropical Indian Ocean. *J. Climate*, **26**, 291–307, doi:10.1175/JCLI-D-12-00113.1.